RSC Advances

PAPER

View Article Online
View Journal | View Issue

Cite this: *RSC Adv.*, 2020, **10**, 38923

Quantitative absorption imaging of red blood cells to determine physical and mechanical properties†

Ratul Paul,[a] Yuyuan Zhou,[b] Mehdi Nikfar,[a] Meghdad Razizadeh[a] and Yaling Liu*[ab]

Red blood cells or erythrocytes, constituting 40 to 45 percent of the total volume of human blood are vesicles filled with hemoglobin with a fluid-like lipid bilayer membrane connected to a 2D spectrin network. The shape, volume, hemoglobin mass, and membrane stiffness of RBCs are important characteristics that influence their ability to circulate through the body and transport oxygen to tissues. In this study, we show that a simple two-LED set up in conjunction with standard microscope imaging can accurately determine the physical and mechanical properties of single RBCs. The Beer–Lambert law and undulatory motion dynamics of the membrane have been used to measure the total volume, hemoglobin mass, membrane tension coefficient, and bending modulus of RBCs. We also show that this method is sensitive enough to distinguish between the mechanical properties of RBCs during morphological changes from a typical discocyte to echinocytes and spherocytes. Measured values of the tension coefficient and bending modulus are 1.27×10^{-6} J m^{-2} and 7.09×10^{-20} J for discocytes, 4.80×10^{-6} J m^{-2} and 7.70×10^{-20} J for echinocytes, and 9.85×10^{-6} J m^{-2} and 9.69×10^{-20} J for spherocytes, respectively. This quantitative light absorption imaging reduces the complexity related to the quantitative imaging of the biophysical and mechanical properties of a single RBC that may lead to enhanced yet simplified point of care devices for analyzing blood cells.

Received 21st June 2020
Accepted 28th September 2020

DOI: 10.1039/d0ra05421f

rsc.li/rsc-advances

1. Introduction

Human red blood cells (RBCs) are non-nucleated cells which are the primary cellular component of blood. Typically shaped like biconcave disks, they have a diameter of 6–8 μm and approximately 2.5 μm thickness. The membrane of the cell is composed of a lipid bilayer and a meshwork of proteins known as the cytoskeleton. The cytoskeleton consists of spectrin and actin filaments that are anchored to the lipid membrane with the help of transmembrane proteins. The membrane helps the RBCs maintain their unique shape with an approximate average volume of 90 femtoliters (fl) and a surface area of 136 μm.[2] Encapsulated by this membrane, the cell is packed with pigments composed of four iron-binding heme groups known as hemoglobin (Hb). The primary function of RBCs is to deliver oxygen and partially absorb carbon dioxide from tissues and exchanging them in the lungs. They do so by a reversible binding-unbinding of oxygen molecules to each heme group. To do this, RBCs must travel through the arteries, veins, and capillaries in the body. These include capillaries with not more than 3–5 μm diameter and endothelial slits with approximately 0.5–1 μm openings. These have apertures that are much smaller than the RBC diameter,[1,2] and thickness. Enduring such a significant level of shear stress and extreme deformation is possible because of their shape, surface area to volume ratio, and mechanical properties of the membrane. Therefore, this comes as no surprise that the physical and mechanical properties of the RBC have been studied extensively.

Impaired shape, Hb concentration, structural and mechanical properties, and count of RBC are observed due to numerous physical disorders.[3] Low hemoglobin concentration or anemia alone is caused by more than seventeen different diseases.[4–8] Patients with cancer, malaria, HIV/AIDS, hookworm, sickle cell disease (SCD), renal diseases, *etc.* are prone to anemia.[9–11] Besides anemia, abnormal shape (echinocyte, teardrop, and sickle cell) and alteration to membrane morphology and mechanical properties can also be attributed to these diseases. Studies have been carried out to associate RBC deformation to several pathological alterations due to malaria,[12–14] sickle cell anemia,[15] hereditary disorders,[16] diabetes,[17] myocardial infarction,[18] *etc.* Traditional blood tests can provide a range of information such as hemoglobin level, RBC and white blood cell (WBC) count, mean corpuscular volume (MCV), *etc.* which are averaged over the whole population of cells in the whole blood. That is why the evaluation of single-cell properties is becoming increasingly popular to increase detection accuracy and develop

[a]*Department of Mechanical Engineering and Mechanics, Lehigh University, Bethlehem, Pennsylvania 18015, USA. E-mail: yal310@lehigh.edu*

[b]*Department of Bioengineering, Lehigh University, Bethlehem, Pennsylvania 18015, USA*

† Electronic supplementary information (ESI) available. See DOI: 10.1039/d0ra05421f

a basic understanding of blood-related disorders by targeting intercellular heterogeneity along with other data. Single-cell hemoglobin and volume measurement are performed in clinical hematology analyzers.[19] Single-cell hemoglobin analysis found that abnormally shaped RBCs in anemia patients, otherwise known as poikilocytes contain elevated hemoglobin.[20] Raman tweezer based single cell hemoglobin measurement has been developed for detecting blood disorders.[21] RBC size and MCV also work as early markers for detecting coronary artery diseases (CAD).[22] Osmotic gradient ektacytometry is an established tool that measures single-cell deformation and MCV without altering the cell volume using Laser-assisted optical Rotational Cell Analyzer (Lorrca) to detect hereditary hemolytic anemia.[23] A classification of healthy and sickle RBCs based on their mechanical properties have been recently reported by Li *et al.*[24] Furthermore, combined single cell hemoglobin, shape and membrane fluctuation measurement has been used to detect irreversible and reversible SCD with a point of care quantitative phase imaging device.[25] Therefore, it is evident that single RBC properties both individually and combined with each other are becoming increasingly popular.

According to an estimation from the World Health Organization (WHO), 30% of the population in the world suffers from anemia, where developing and underdeveloped regions like Africa and South-East Asia are the most prevalent. The widespread nature of anemia has inspired researchers to develop point-of-care devices to analyze blood samples[26–30] for early detection. Recent advancements in the smartphone industry have seen devices containing high-resolution cameras with low light capability. Their processing power has also increased multiple times over the past 5 years. This makes smartphones the perfect devices for point-of-care analytical biosensing.[31,32] The use of microfluidic channels has increased the flexibility and scope of point of care smartphone imaging.[33] Capable of efficient bright-field and fluorescence imaging, smartphones are used in malaria and sickle cell disease detection.[34,35] But most of these examples lack single-cell evaluation of RBCs.

Single-cell characterization of RBC includes micropipette aspiration,[36–38] optical tweezers,[39–44] electric field deformation,[45] atomic force microscope (AFM),[46–52] optical quantitative imaging,[53–60] and microfluidic-based deformation and recovery analysis.[61–66] These quantitative methods can measure RBC volume, hemoglobin mass, surface area, cytoplasmic viscosity membrane tension coefficient, bending modulus, Young's modulus, *etc.* Recently optical imaging-based non-contact methods to predict biophysical and mechanical properties of RBC have become popular. RBC membrane fluctuation data has been widely used to measure the mechanical properties of RBC by recording reliable fluctuation data with quantitative phase imaging (QPI).[56,67–70] QPI based methods have even been used to understand the interaction between the phospholipid membrane and the cytoskeleton.[71–73] Multiwavelength transmission spectroscopy has been used to measure mean cell hemoglobin (MCH) and mean cell volume (MCV).[11] A combination of QPI and amplitude imaging method with light sources of multiple wavelength has been used to measure the hemoglobin mass and volume simultaneously.[74] The refractive index of the RBC has been tied with the phase change in phase microscopy to measure hemoglobin and volume of RBC simultaneously with digital holographic microscopy (DHM).[75] While it is true that QPI and DHM provides a non-invasive and quantitative measurement of RBC properties, these measurement setups are complicated, bulky, expensive, and susceptible to mechanical vibration.[76] Typically, a light interference or phase difference-based imaging method requires sophisticated parts such as prisms, beam-splitters, light modulators, PZT drivers, *etc.* which are generally expensive and require precise positioning. Such a QPI setup may cost up to USD 30,000. Recently, a modified QPI unit (QPIU) was developed and tested in sickle cell detection in Tanzania[25] which is comparatively more compact and cheaper. The QPIU costs 10 times less than a standard QPI setup[25] but still requires three sensitive optical parts (two linear 45° polarizers and one Rochon prism). Developing a cheaper alternative for reliable measurement of RBC properties can have applications as an affordable point of care diagnosis tools in distant and underdeveloped countries.

In this study, we present a simple setup to determine the Hb concentration, total volume, and membrane mechanical properties of RBC through light absorption imaging. Light absorption imaging has never been used in such a complete evaluation of RBC properties. It has also been shown that this method can accurately measure the aforementioned properties of RBCs in different morphological states. Furthermore, the membrane fluctuation of a fixed RBC was analyzed to check if the method can differentiate among various fluctuation modes due to the stiffening of the RBC cytoskeleton. Characterization of RBC properties through such a simple and inexpensive optical setup made of two LEDs may help develop more affordable, accurate, and efficient disease detection.

2. Materials and methods

2.1. Theory

The height and Hb mapping of a single RBC has been measured with the Beer–Lambert law of light absorption with the procedure proposed by Schonbrun *et al.*[54] Beer–Lambert law linearly relates the absorption of light through a mixture or substance to its properties. Light attenuation through a single substance will exclusively be caused by light absorption. But if there are multiple substances in the optical path, light scattering will contribute to the attenuation due to the mismatch in the refractive index.[77] The presence of an RBC in the buffer for this experiment loses its homogeneity due to the mismatch in the refractive index of the RBC and the buffer. To offset this mismatch, the refractive index of the buffer has been increased by creating 33 gdL^{-1} bovine serum albumin (BSA) solution with phosphate buffer saline (PBS). This method matches the concentration of BSA with the documented average concentration of Hb in an RBC, as BSA and Hb have similar refractive index.[78]

The height has been measured with the help of dye exclusion absorption imaging. When a dye solution efficiently absorbs light of a certain wavelength, the presence of a cell in the optical

path will increase the light transmission by removing the dye particle from the optical path. A graphical representation of the principle has been shown in Fig. 1a. For this experiment, a non-membrane permeable dye acid blue 9 (AB9)[79] has been used which has an absorption peak at 630 nm. Unlike the height measurement, the Hb mass of the RBC has been measured with direct absorption of light by Hb. As the experiments have been conducted under ambient conditions, we assumed that the Hb in the RBC is oxygenated. The peak absorption of oxygenated Hb is at 412 nm which is known as the Soret band.

A Microfluidic channel with a known channel height has been used to place the RBCs in the optical path. For our experiment, the channel height was 6.5 μm. The channel profile obtained from a profilometer has been shown in Fig. 1b. Using a combination of 630 nm and 405 nm LED, light absorption images of the channel with and without an RBC were captured.

The acquired images contain the pixel values that represent the spatial light intensity. The image of the channel without the RBC is used as the background or reference intensity. The red channel in the absorption image is used to measure the height mapping of the RBC by:

$$h = \log_e\left(\frac{I^{red}_{cell}}{I^{red}_{background}}\right) \Big/ \alpha_{AB9} \quad (1)$$

The blue channel, on the other hand, is used to measure the Hb mapping of the RBC by:

$$m = \log_e\left(\frac{I^{blue}_{cell}}{I^{blue}_{background}}\right) \Big/ (-\alpha_{Hb}) \quad (2)$$

where h and m represent the per-pixel height and mass mapping. I^{red}_{cell} and $I^{red}_{background}$, represents the per-pixel intensity of the red channel of the image with and without the RBC. I^{blue}_{cell} and $I^{blue}_{background}$ represents the per-pixel intensity of the blue channel of the image with and without the RBC. α_{AB9} and α_{Hb} represents the absorption coefficient of AB9 and Hb and their values are 0.2 μm^{-1} and 4.06×10^5 M^{-1} cm^{-1} respectively.[54] The per-pixel height values are then multiplied with the pixel size to find per pixel volume for the RBC. Summing the per pixel mass and volume over all the pixels gives us the total mass and volume of the RBC.

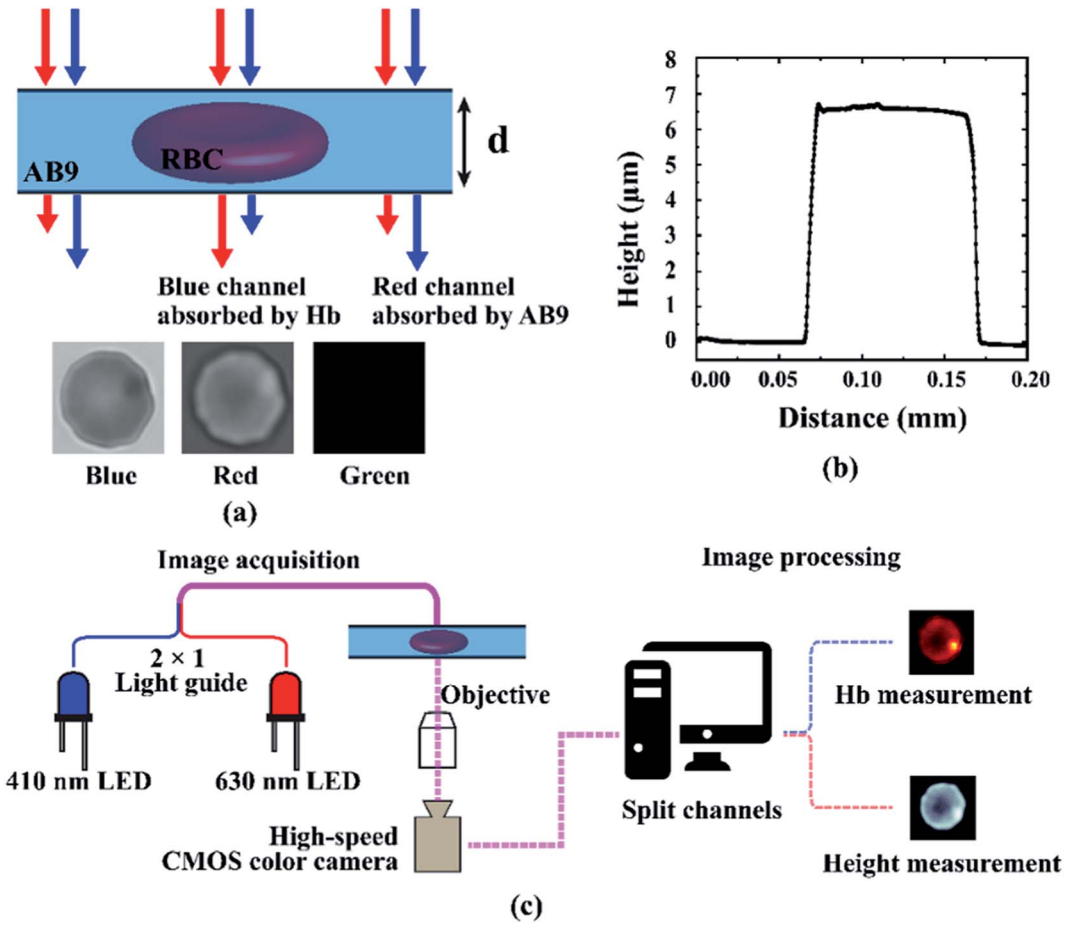

Fig. 1 (a) Graphical representation of the light absorption of AB9 and RBC. The intensity of the blue light decreases while passing through an RBC. The intensity of the red light, on the other hand, decreases while passing through the AB9 solution. Three channels are shown that are extracted from a typical color image. As there is no green light in the source, the green channel is completely dark. (b) Profilometer scan of the channel used for this experiment. (c) A simple schematic diagram of the experimental setup. The setup can be divided into image acquisition and processing.

The tension coefficient and bending modulus of the RBC membrane has been calculated from the height fluctuation data based on the well-known Helfrich Hamiltonian[56,80–83] and formalism of coherence in the space-frequency domain developed by Mandel and Wolf for electromagnetic field fluctuation.[55,84,85] According to Helfrich Hamiltonian, the required energy to stretch and bend a bilayer membrane can be defined by

$$F = \int \mathrm{d}A \left[\frac{1}{2}\kappa\left(\nabla^2 \Delta h^2\right) + \frac{1}{2}\sigma(\nabla \Delta h)^2 \right] \quad (3)$$

where Δh is the deflection of a point from its equilibrium position, A is the area of the membrane, σ is the tension coefficient and κ is the bending modulus. The integral represents the sum over the whole membrane area. Per-pixel deflection or fluctuation of the membrane is measured by determining and comparing the height mapping of the individual frame from an image sequence. For this experiment, 500 frames were recorded for each sample at 100 fps. A set of 100 frames were taken to measure the equilibrium height mapping of the RBC by averaging the mappings over time while each frame was compared to the equilibrium mapping to determine the height fluctuation $\Delta h\ (x, y; t)$. If we consider the membrane to be in thermal equilibrium, it is convenient to assign the energy $k_\mathrm{B}T/2$ to each q-mode and express eqn (3) as static membrane fluctuation spectrum

$$\Delta h^2(q) = \frac{k_\mathrm{B}T}{A} \times \frac{1}{\sigma q^2 + \kappa q^4} \quad (4)$$

where, k_B is the Boltzmann constant and $T = 298\mathrm{K}$ is the room temperature. $\Delta h^2(q)$ is the time average of squared deflection value for each pixel in the wave vector (q) and frequency (ω) domain. Here $q = |q| = \sqrt[2]{{q_x}^2 + {q_y}^2}$ where $q_x = 2\pi n_x/L_x$ and $q_y = 2\pi n_y/L_y$, n and L being the pixel number and length in x and y direction in the spatial domain. $\Delta h(q)$ is calculated by taking the Fourier transformation of $\Delta h\ (x, y; t)$ in time and space. Eqn (4) can be separated into two limiting cases based on whether the fluctuation is dominated by the membrane tension or the bending modulus. The lower wave vector region is dominated by membrane tension where q values can be fitted in the equation

$$\Delta h^2(q) = (k_\mathrm{B}T/A) \times (1/\sigma q^2) \quad (5)$$

to determine the membrane tension coefficient (σ). The higher wave vector region, on the other hand, is dominated by the bending modulus where

$$\Delta h^2(q) = (k_\mathrm{B}T/A) \times (1/\kappa q^4) \quad (6)$$

can be fitted to determine the membrane bending modulus (κ). Previous studies investigating the thermal fluctuation of RBCs have defined the tension dominated region to be in $q < 6$ (ref. 86) and $q < 10$ (ref. 87) while the bending modulus dominated region had been defined to be in $18 > q > 7$ (ref. 86) and $q > 10$ (ref. 87).

2.2. Sample preparation

Blood from healthy donors was collected and sent from the University of Maryland School of Medicine. The human blood with clinical hemoglobin analyzer measurements was collected from Lampire Biological Laboratories (Coopersburg, PA, USA). The sample collection process has followed approved institutional review board protocols with donors providing informed consent. The experiment for the discocyte and spherocyte was run within 48 hours of the blood collection when no significant alteration of RBC shape was observed. A ten days old blood sample received from the University of Maryland School of Medicine and stored in a 4 °C refrigerator has been used to collect the data for echinocytes. Many RBCs in the old sample had irregular spiky shape due to hypothermic storage[88,89] which were considered as echinocytes by visual inspection. To prepare RBC pellet from the whole blood, standard washing and dilution procedure was followed. 50 μl of human blood was rinsed with 2 ml of PBS and centrifuged at 500 rcf for 10 minutes. The supernatant was removed before the remaining RBC at the bottom of the centrifuge tube was resuspended in 2 ml of PBS and centrifuged at 500 rcf for 10 minutes again. After removing the supernatant again, the RBC was resuspended in 2 ml of isotonic (for discocyte) or hypotonic (for spherocyte) BSA and AB9 solution and were taken into a syringe for the experiment. The isotonic BSA and AB9 solutions were made by suspending the solid BSA and AB9 in 1× PBS at 33 g dl^{-1} and 0.8 g dl^{-1} w/v concentrations. The hypotonic solution was prepared by adding DI water to the 1× PBS before making the BSA and AB9 solution to achieve a 220 mOs mol per L osmolarity. The hypotonic medium caused the RBCs to swell and take a more sphere-like shape than the usual disc-like shape. The sample had 90 000 RBCs per mm^3 concentration.

RBCs for the confocal scanning were prepared by first separating the RBCs following the procedure mentioned above. The washed RBCs were resuspended in PBS and stained with 10 μl Vybrant™ DID for 30 minutes at 37 °C. The RBCs were washed again twice to get rid of the suspended dye. The RBCs were fixed with 1% glutaraldehyde for five minutes before washing and resuspending them to PBS again. 100 μl of the RBC sample was placed on a poly-L-lysine functionalized gridded coverslip and was let to sit for two minutes. The coverslip was functionalized by poly-L-lysine by first washing it with ethanol and distilled water ($\mathrm{dH_2O}$) and letting them dry. Then, 150 μl of poly-L-lysin solution was applied to the center of the coverslip for 5 minutes and washed three times with $\mathrm{dH_2O}$ and was air-dried. The excess sample was washed out with a slow stream of PBS and immediately scanned with a Nikon C2+ confocal microscope. The gridded coverslip was used to easily track the same RBCs to measure the height mapping using the light absorption method. After the confocal measurement, the excess PBS remaining over the glass was removed with a pipette and the samples were covered with a PDMS cover having a 6.5 μm clearance and an inlet and outlet. Isotonic BSA and AB9 solutions were then slowly inserted through the inlet which created a uniform sample thickness of 6.5 μm ready for absorption imaging.

2.3. Fabrication of microfluidic device

For this experiment, a known distance of sample (represented as 'd' in Fig. 1a) is required to determine the RBC thickness by subtracting the distance of BSA and AB9 solution measured by light absorption from the known distance. This distance should also be consistent between multiple measurements. Otherwise, the image processing code will need to be changed to account for this change. To maintain a constant length of the light path and facilitate the inlet and outlet of the flow, micron-sized channels have been used. The channels used for our absorption imaging were 6.5 μm tall, 100 μm wide, and 10 mm long. The size of the channel has been measured with a profilometer and presented in Fig. 1b. These relatively simple channels were made with polydimethylsiloxane (PDMS) molding. The master negative pattern was developed with photolithography at The Center for Photonics and Nanoelectronics (CPN) at Lehigh University using the Suss MA6/BA6 mask aligner. SU8 2007 photoresist (52.50% solid) was diluted with cyclopentanone at a 25 : 4.1 volume ratio to achieve similar viscosity as SU8 2005 (45% solid). The mixture was then spin-coated at 2000 rpm on a silicon wafer before the UV exposure to achieve 6.5 μm channel height. Sylgard 184 PDMS was mixed with the curing agent at a ratio of 10 : 1 and poured over the photoresist master. After degassing the PDMS for 2 hours, it was let to cure overnight. Holes were punched out of the PDMS channel before attaching it to a large coverslip with oxygen plasma treatment. The RBC sample should naturally settle over the slide surface after a few minutes. Frames captured before the RBC settles down can be used as the background frame as long as the region of interest (ROI) of the camera is not changed.

2.4. Optical imaging

High power LEDs were used for the illumination of the sample. For the red light, LUXEON Z Red LEDs of 1300 mW at 500 mA with a wavelength range of 624–634 nm were used. LUXEON Z UV LEDs of 2700 mW at 500 mA W was used for the blue light which has a wavelength range of 405–410 nm. Four LEDs of each color were mounted on a Saber Z5 20 mm base. Both LEDs have a full-width half-maximum (FWHM) of approximately 15 nm. The LEDs were focused on the optical light guide with Carclo 8° 20 mm concentrator. The samples were magnified using a 100 × 1.25 NA Olympus SPlan oil emersion objective mounted on an Olympus IX70 microscope. 500 images were captured per image sequence using XIMEA CB120CG-CM color CMOS camera at 12 bit mode with an exposure time of 100 μs and 100 fps recording speed. Captured images had an area of 0.00056 μm^2 per pixel. The sample was loaded in a 1 ml lure lock syringe and connected to the microfluidic channel using a 1/32″ inner diameter polyurethane tubing before loading the syringe in the syringe pump. The movement of the sample was controlled by a Just Infusion™ NE-300 syringe pump. By turning the syringe pump on and off, new RBCs were introduced to the ROI of the camera while keeping the background constant. Turning the syringe pump off also quickly makes the RBCs stagnant and thus gets rid of any bulk movement of the RBC that might result in erroneous calculation of height fluctuation. The concentration of the RBCs in the sample was low enough to avoid a significant number of RBCs getting attached to each other.

2.5. Data analysis

All the image processing in this experiment was done semi-automatically with MATLAB R2018b.

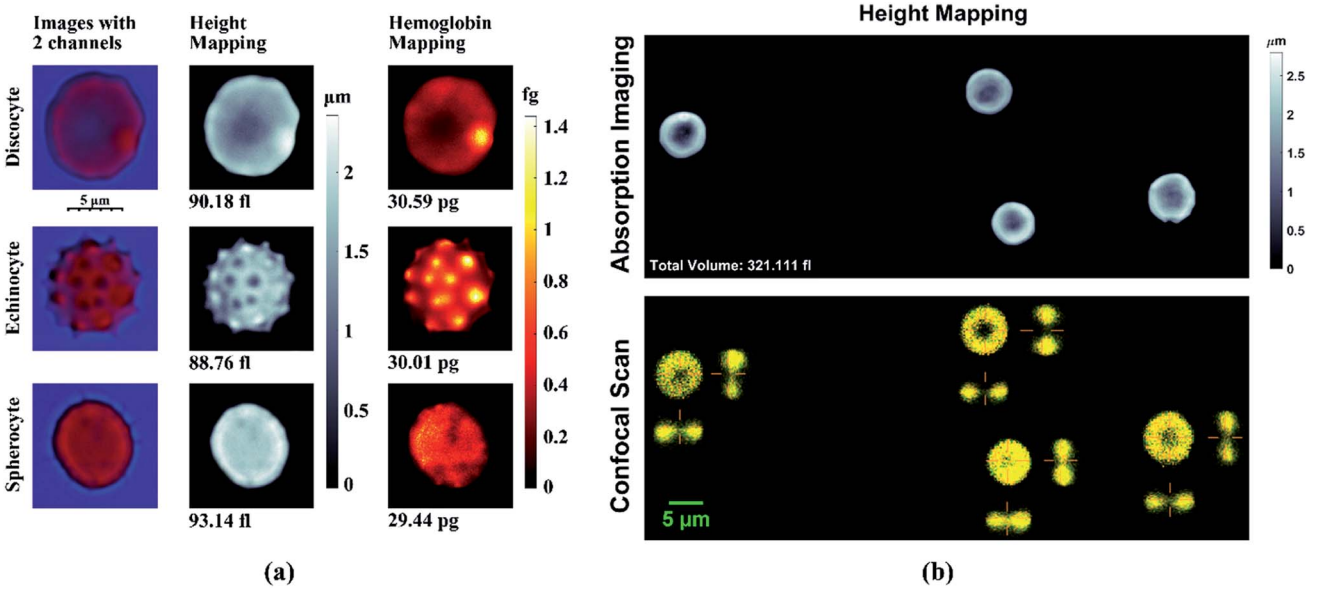

Fig. 2 (a) Hemoglobin mass and height mapping of discocyte, echinocyte, and spherocyte measured by absorption imaging. The total Hb mass and volume are 30.59 pg, 30.01 pg, 29.44 pg and 90.18 fl, 88.76 fl, 93.14 fl respectively. The maximum height in the height mapping is 2.8 μm. The scale in the figure is applicable for all three RBCs. (b) Comparing the height mapping measured by light absorption imaging to that of confocal scanning.

3. Results

First, the Hb and height mapping of different morphologies, discocyte (DC), echinocyte (EC), and spherocyte (SP) of RBC have been computed with quantitative absorption imaging. The total Hb mass and volume for DC, EC, and SP measured from the experiment are 30.59 pg, 30.01 pg, 29.44 pg, and 90.18 fl, 88.76 fl, 93.14 fl respectively. For different morphologies of RBC, the total Hb mass and volume agrees well with previous studies.[54,90] The results are shown in Fig. 2a.

Fig. 2b shows a comparison of the height profile of 4 RBCs measured with light absorption and confocal scanning to validate the accuracy of this method. The two cross-sectional views of the RBCs are shown along with the top view of the confocal scan. The height mapping through light absorption method matches well with the cross-sectional height measurement of the RBCs with a confocal microscope. Light absorption imaging has been used as a cytometry to measure Hb mass and volume of moving RBCs by Schonbrun *et al.*[54] However, independent Hb mass and volume measurement for the DC, EC, and SP samples for 500 sequential images show a normal distribution with a standard deviation of 1.18 pg, 0.89 pg, 1.26 pg, and 2.80 fl, 2.12 fl, 0.46 fl. Fig. 3 shows that the calculated average total Hb mass and volume for DC, EC, and SP from 500 frames maintain are 30.64 pg, 30.67 pg, 29.54 pg, and 91.82 fl, 87.16 fl, 93.99 fl. This provides statistically accurate measurements for RBC physical properties.

A comparison has been made between the mean corpuscular volume (MCV), mean corpuscular hemoglobin (MCH), and mean corpuscular hemoglobin concentration (MCHC) measured with the light absorption method and clinical hemoglobin analyzer which is shown in Table 1. 150 RBCs were analyzed to measure a statistically accurate MCV, MCH, and MCHC with the light absorption imaging method. It shows that the results from this experiment are in good agreement with the clinically measured data. Thus, this method can be used to acquire statistical data of RBC physical properties like that of a clinical hemoglobin analyzer. Fig. 4 shows the scatter plot of the hemoglobin mass and hemoglobin concentration *vs.* the volume of each RBCs measured. As expected, the hemoglobin concentration in RBC shows a nearly constant level in a healthy RBC sample.[91] The wide range of slope for a 95% confidence level shows that there is no strong correlation between the hemoglobin concentration and volume of RBCs. However, RBCs from a patient of hereditary spherocytosis (HS) have been seen to exhibit a much wider hemoglobin concentration band in a previous study.[91] Thus, the distribution of hemoglobin concentration can give us the initial sign of hereditary spherocytosis (HS). As the hemoglobin concentration is constant in healthy RBCs, the positive correlation between RBC volume and total hemoglobin mass was expected. A narrow range of the slope indicates a strong correlation between hemoglobin mass and volume in a single RBC.

Table 1 MCV, MCH, and MCHC comparison between this experiment and clinically measured data

	This experiment		Clinical measurement
	Mean	Standard deviation	
MCH (pg)	29.13	3.58	28.7
MCV (μm^3)	84.59	7.5	84
MCHC g dl^{-1}	34.49	3.61	34

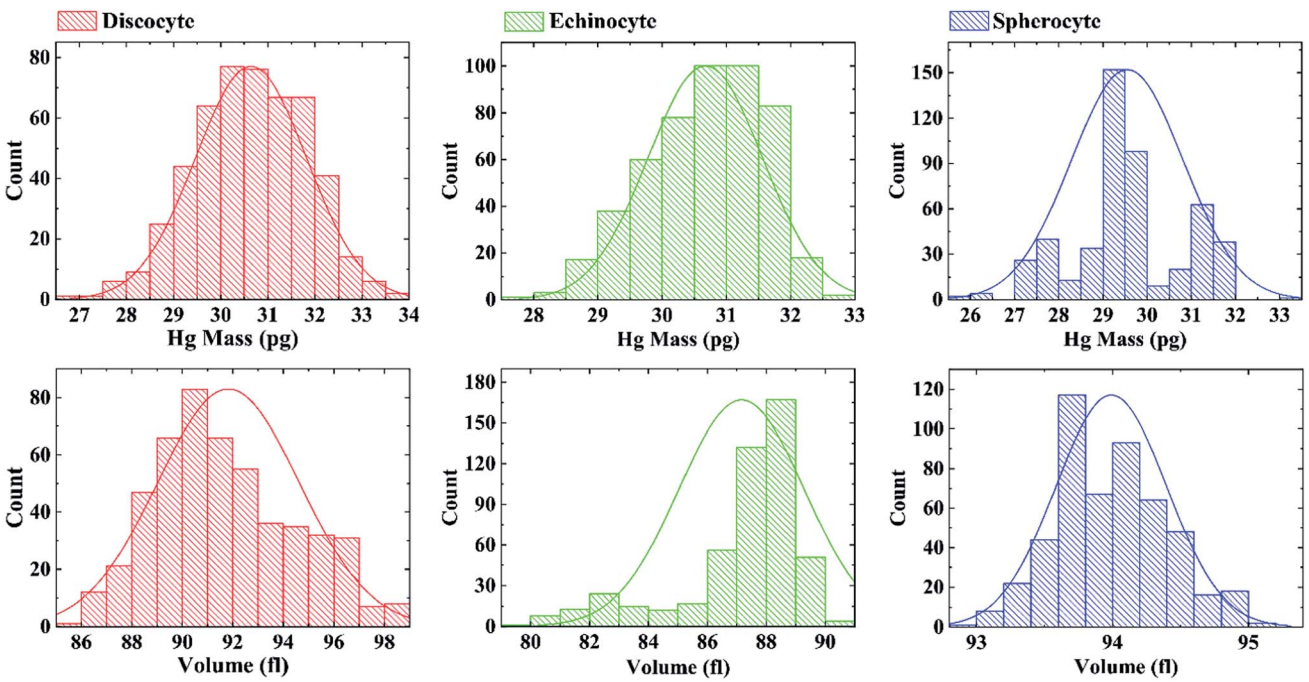

Fig. 3 Distribution of Hb mass and volume for discocyte, echinocyte, and spherocyte measured for 500 frames.

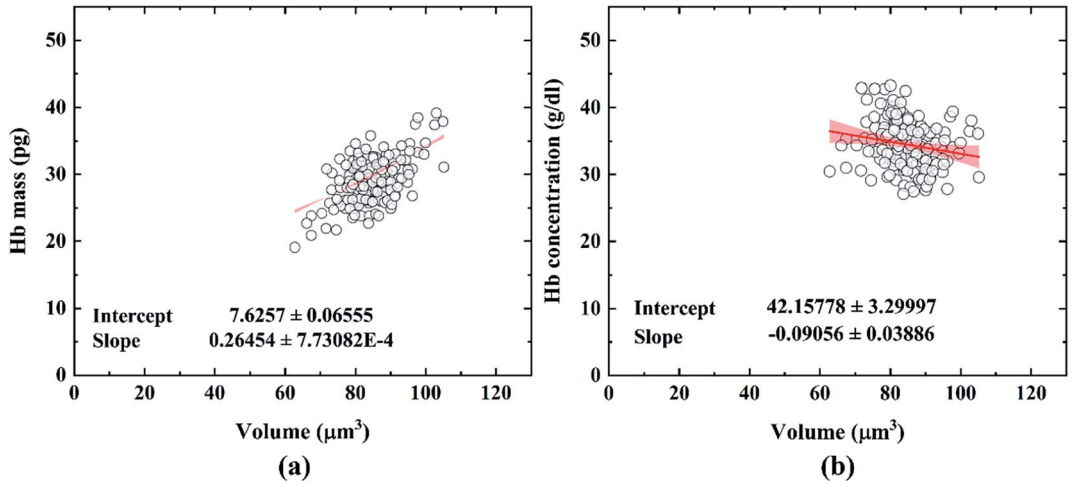

Fig. 4 Plot of the (a) Hb mass *vs.* RBC volume and (b) Hb concentration *vs.* volume for 150 human RBCs. The red solid line in each figure represent a linear fit and the shaded region shows the range of slope that covers 95% confidence level.

To predict the mechanical properties of the RBC membrane with light absorption imaging, image sequences have been analyzed for the three types of RBC morphologies and RBC fixed with 40 μM glutaraldehyde. For this experiment, the transverse fluctuation has been measured by subtracting the height mapping for each frame from the average height mapping for 100 consecutive frames. So, unlike the measurement of Hb mass and volume, the fluctuation measurement is not independent of the other frames. Caution must be given to avoid erroneous data due to the radial fluctuation of the membrane.

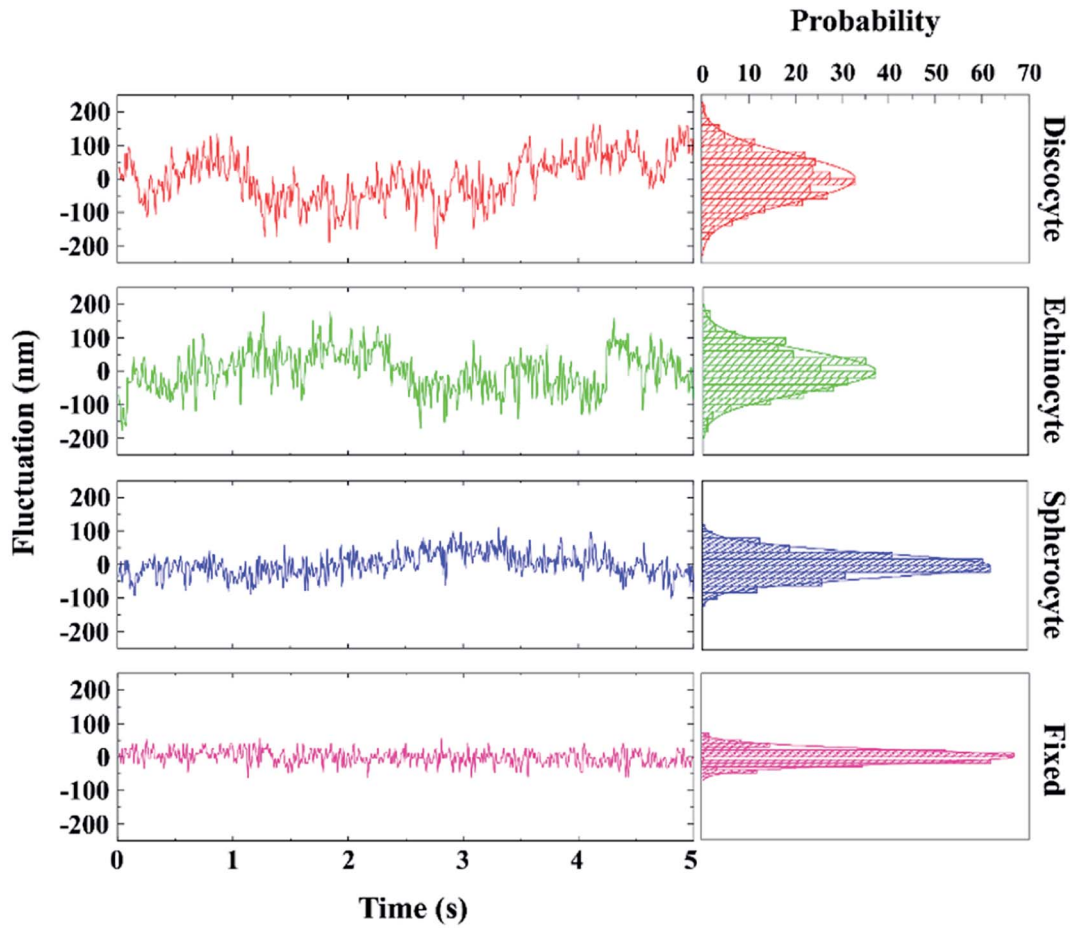

Fig. 5 Fluctuation distribution of different types of RBCs. As the RBC stiffens, the fluctuation starts showing a more centered distribution with a significantly smaller standard deviation.

The contour of the cell has been tracked with automatic edge detection prior to the fluctuation analysis. The edge fluctuation has been shown in the ESI.† The region of interest (ROI) for the transverse fluctuation is created by masking out the region created from the edge fluctuation. Randomly selected pixels on the membrane show that the fluctuation in the membrane follows an almost symmetrical normal distribution).

The fluctuation distributions for different types of RBCs are summarized in Fig. 5. The DC shows the widest range of membrane fluctuation. The EC has similar but slightly less membrane fluctuation than the discocyte which is a sign of a stiffer membrane. In comparison with the DC and EC, the SP and fixed RBC show significantly weaker fluctuation with a much slender distribution. A similar trend has been observed among healthy and modified RBCs in previous studies.[73,92–96] The differences in the membrane fluctuation resulted in reduced root mean squared normal displacement $\sqrt{\langle \Delta h(x,y)^2 \rangle}$ that are shown in Fig. 5. The braces indicate time averaging.

This provides a qualitative expression of the differences between RBC membrane spatial heterogeneity and mechanical property. Using the equipartition theorem for thermally equilibrium membrane fluctuation, effective spring constant (k_e) of the membrane can be determined from the average spatial fluctuation data by the formula $k_e = k_B T/\langle \Delta h^2 \rangle$. For a typical DC, effective spring constant $k_e = 1.9$ μN m^{-1} was measured from RBC flickering by Park *et al.*[57] In their study, diffraction phase microscopy (DPM) was used to measure $\sqrt{\langle \Delta h^2 \rangle}$ values over the morphological transition from DC to SP (46 nm for DC, 34 nm for EC, and 15 nm for SP). The calculated $\sqrt{\langle \Delta h(x,y)^2 \rangle}$ from the light absorption imaging in this experiment are 47.8 nm for a DC, 34.7 nm for an EC, 19.2 nm for an SP, and 14.7 nm for a fixed RBC (Fig. 6) which accounts for an effective spring constant of 1.79 μN m^{-1} for DC. Our results agree well with the qualitative values in the above-mentioned study. The instantaneous fluctuation mappings are available in the ESI.† The quantitative analysis of membrane fluctuation however is more convenient in the spatial Fourier space. As mentioned in the theory section, the spatial Fourier transform of the membrane fluctuation is expressed by the wave vector (q) by eqn (4). The fluctuation amplitude at different wave vector (q-mode) represents a different mode of membrane behavior in terms of its mechanical properties. So, the $\Delta h(q)$ was measured from the average spatial fluctuation data $\Delta h(x,y)$ by Fourier transformation. The radially averaged $\Delta h^2(q)$ values were then plotted against the wave vector. Fig. 7(a) represents the plot for DC in the linear axis while Fig. 7(b) shows the same plot in the logarithmic scale. In a linear scale, the abrupt change in the slope of fluctuation spectra clearly shows the transition of the fluctuation amplitude from the region suppressed by the membrane tension to the region suppressed by the bending modulus.[81] The two regions show a power low behavior for q^{-2} and q^{-4}. The coefficient for q^{-2} and q^{-4} has been measured by fitting the plot with eqn (5) and (6) in the range of $q < 5$ and $5 < q < 18$ respectively. The predicted values of tension coefficient (σ) and bending modulus (κ) for DC from the fitting are 1.27 ± 0.09

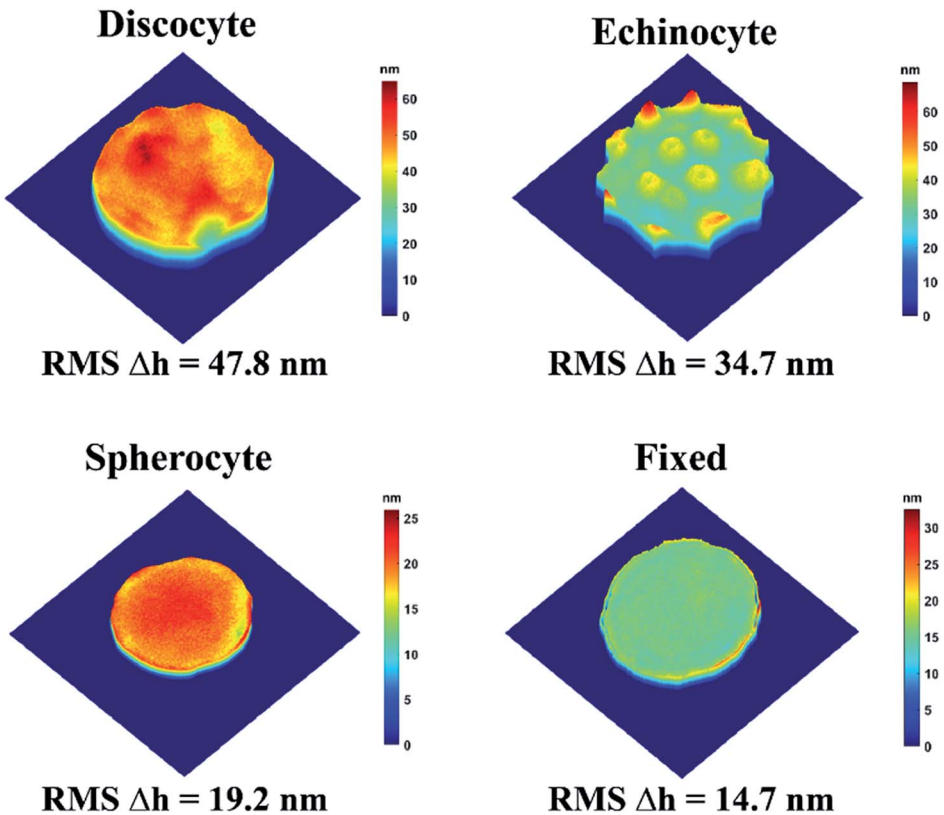

Fig. 6 The root means square of fluctuation for different types of RBCs calculated from the height mapping.

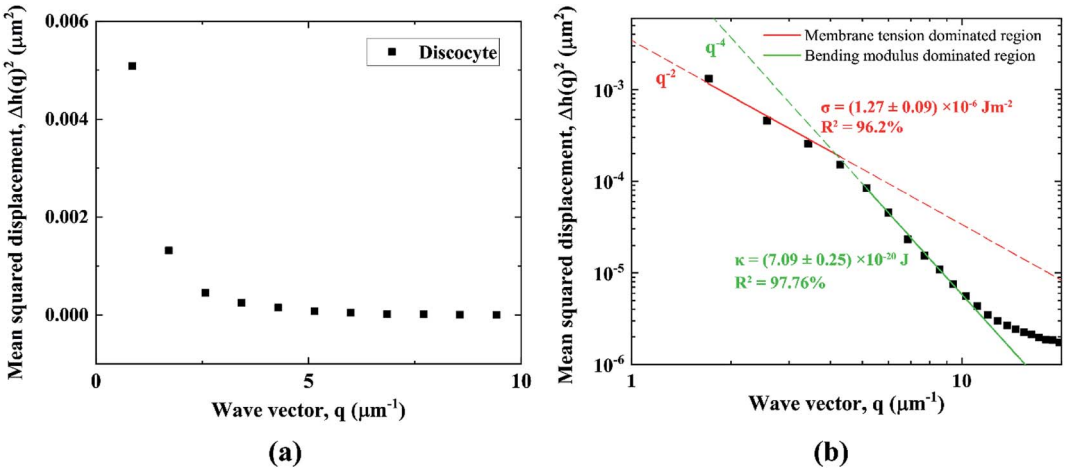

Fig. 7 Mean squared displacement plot as a function of wave vector for discocyte in (a) linear scale, (b) logarithmic scale for wave vector $1 < q < 20$. (b) shows the fitting of the plot in q^{-2} and q^{-4} region to calculate the membrane tension coefficient and bending modulus for a 95% confidence level.

$\times 10^{-6}$ J m^{-2} and $7.09 \pm 0.25 \times 10^{-20}$ J.

The tension coefficient and bending modulus for EC, and SP have been derived similarly from the $\Delta h^2(q)$ *vs.* q plot as shown in Fig. 8a. The fixed RBC shows significantly reduced fluctuation similar to that in the previous study.[56] The fluctuation does not show any q^{-2} mode in the small wave vector region. The larger wave vector region with smaller fluctuation accounts for fluctuation much smaller than the average bilayer-cytoskeleton distance of (30 nm).[83]

Cytoskeleton stiffening and the interaction between membrane and cytoskeleton has a smaller effect in this region. Therefore, bending modulus is less effected overall by the morphological changes in RBCs. The tension coefficient and bending modulus for EC and SP from our experiment are $4.80 \pm 0.34 \times 10^{-6}$ J m^{-2} and $7.70 \pm 0.78 \times 10^{-20}$ J. and $9.85 \pm 0.29 \times$

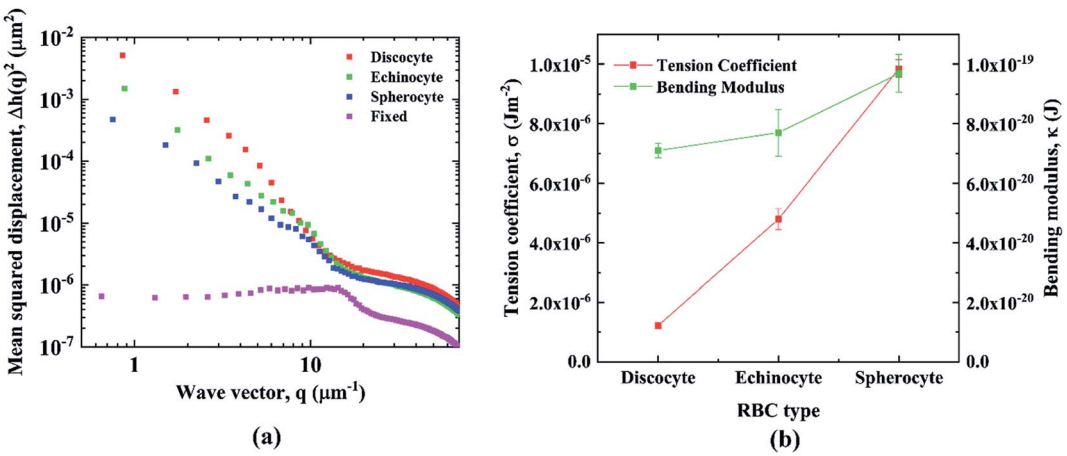

Fig. 8 (a) Mean squared displacement plot as a function of wave vector for DC, EC, SP, and fixed RBC. (b) Comparison of tension coefficient and bending modulus of DC, EC, and SP.

Table 2 Comparison of tension coefficient and bending modulus measured from our experiment with previously reported values

		This work	Previous work
Tension coefficient, σ ($\times 10^{-6}$ J m^{-2})	DC	1.27 ± 0.09	1.50 ± 0.2 (ref. 56), 0.5–1.2 (ref. 83)
	EC	4.80 ± 0.34	4.05 ± 1.1 (ref. 56)
	SP	9.85 ± 0.29	8.25 ± 1.6 (ref. 56)
Bending modulus, κ ($\times 10^{-20}$ J)	DC	7.09 ± 0.25	5.60 ± 0.06 (ref. 56), 2.30 ± 0.69 (ref. 57)
	EC	7.70 ± 0.78	9.12 ± 0.06 (ref. 56), 3.94 ± 1.31 (ref. 57)
	SP	9.69 ± 0.62	8.41 ± 0.06 (ref. 56), 9.80 ± 2.7 (ref. 57)

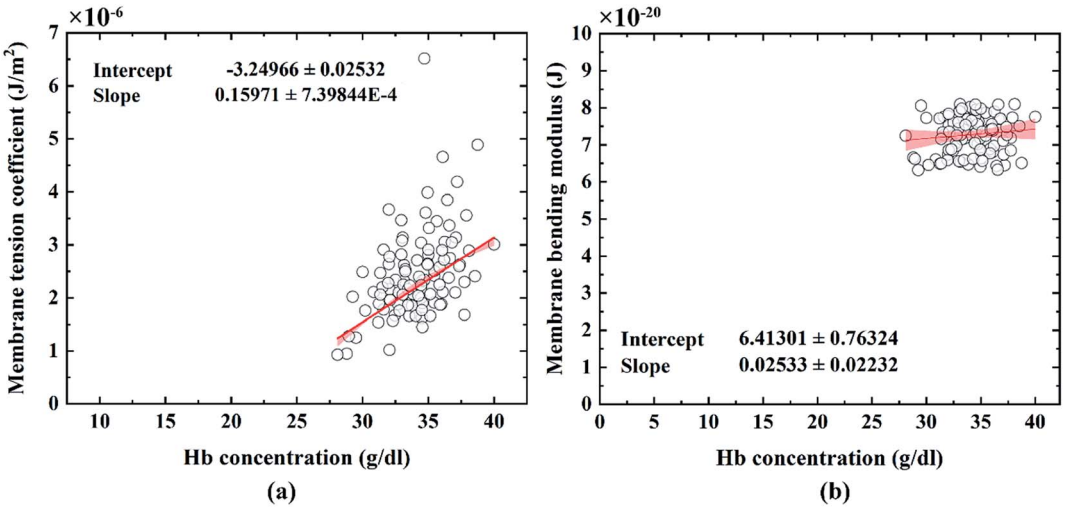

Fig. 9 2D scatter plot of (a) Hb concentration and membrane tension coefficient and (b) Hb concentration and membrane bending modulus. The red line in each figure represents a linear fit and the shaded region represents the range of slope that covers 95% confidence level.

10^{-6} J m^{-2} and 9.69 ± 0.62 × 10^{-20} J respectively. The results show a large increase of 87.6% in the tension coefficient while a comparatively smaller increase of 26.7% in bending modulus due to morphological transition in RBC from DC to SP. The results agree well with previous studies as seen in Table 2.

A correlation between hemoglobin concentration and membrane tension coefficient/bending modulus is shown in Fig. 9. The bending modulus is responsible for maintaining the shape of the RBC membrane and remains nearly unchanged with a change in hemoglobin concentration (Fig. 9b). This supports previous reports that RBC bending modulus do not get significantly affected by hemoglobin concentration both in normal and sickle cells.[97,98] Membrane tension on the other hand is more directly related to the stiffness of the cell and shows a strong positive correlation with hemoglobin concentration (Fig. 9a). It can be explained by the increased cytoplasmic viscosity that results from increased hemoglobin concentration.[91]

4. Conclusion

This study shows that the physical and mechanical properties of RBC can be reliably measured with light absorption imaging by a simple two-LED setup using a moderately high-speed color camera. This method is sensitive enough to differentiate between different morphological states of RBC and shows significant relevance to previously reported values. This method is notably cheaper and less complex compared to the other non-contact quantitative imaging methods such as QPI, DHM, or diffraction phase microscopy (DPM), and can directly measure both hemoglobin mass and structural properties of RBCs in a much more straightforward manner. The total cost for the setup in this experiment is only USD 175 (see appendix on Bill of Materials). It is a separate unit that can be installed over a standard inverted microscope. The unit does not contain any sensitive or fragile optical element and costs several times less than the QPIU setup. Such a simple setup can be utilized in the development of cheap and effective point of care blood analyzer and disease detection kit.

Appendix

The bill of materials (BOM) for the experimental setup has been given in the table below.

Component	Units	Unit price (USD)	Total per component (USD)
1. 4 Series connected LUXEON Z 405 nm Ultraviolet LEDs on a Saber Z5 20 mm base – 2700 mW @ 500 mA	1	35.4	35.4
2. 4 Series connected LUXEON Z Red LEDs on a Saber Z5 20 mm base - 208 lm @ 500 mA	1	13	13
3. Carclo 20 mm Clear Hex Optic Holder – Pegged Feet	2	0.5	1
4. Carclo 8° 20 mm Concentrator Beam Optic	2	1.8	3.6
5. Tri Tronics Fiber Optics Barrel Tip Light Guide/BF-E-36AP	1	87.72	87.72
6. 3D printed LED enclosure (Printed in The Wilbur Powerhouse – Lehigh University in an Ultimaker 2 with PLA)	1	5	5
7. Nxtop Aluminum Heat Sink Heatsink Module Cooler Fin 100 mm (L) × 69 mm(W) × 36 mm(H)	1	11	11
8. Standard breadboard, resistor, potentiometer, led, jumper wire set	1	8	8
9. CTS Industrial 24mmDiameter 5 Watt, Wirewound rotart potentiometer (100 ohm)	1	5.34	5.34
10. CTS Industrial 24mmDiameter 5 Watt, Wirewound rotart potentiometer (250 ohm)	1	5.34	5.34
Total			175.4

Conflicts of interest

There are no conflicts to declare.

Acknowledgements

This work was supported by the National Institutes of Health (NIH) grant number R01HL131750, and the Pennsylvania Infrastructure Technology Alliance (PITA) grant. This project is also funded, in part, under a grant with the Pennsylvania Department of Health. The Department specifically disclaims responsibility for analyses, interpretations, or conclusions. The authors would like to thank the donors participating in this study for providing blood samples. Dr Zhongjun Wu and Zachary Berk from University of Maryland for coordinating the clinical sample and data collection.

References

1 S. Guido and G. Tomaiuolo, Microconfined flow behavior of red blood cells *in vitro*, *C. R. Phys.*, 2009, **10**, 751–763.
2 C. H. Wang and A. S. Popel, Effect of red blood cell shape on oxygen transport in capillaries, *Math. Biosci.*, 1993, **116**, 89–110.
3 Y. Yawata, *Cell membrane: the red blood cell as a model*, Wiley-VCH, 2003.
4 K. M. Nair, S. Fernandez-Rao, B. Nagalla, R. V. Kankipati, R. Punjal, L. F. Augustine, K. M. Hurley, N. Tilton, K. B. Harding, G. Reinhart and M. M. Black, Characterisation of anaemia and associated factors among infants and pre-schoolers from rural India, *Public Health Nutr.*, 2016, **19**, 861–871.
5 B. T. Kadima, J. L. Gini Ehungu, R. M. Ngiyulu, P. M. Ekulu and M. N. Aloni, High rate of sickle cell anaemia in Sub-Saharan Africa underlines the need to screen all children with severe anaemia for the disease, *Acta Paediatr.*, 2015, **104**, 1269–1273.
6 C. Menendez, A. F. Fleming and P. L. Alonso, Malaria-related anaemia, *Parasitol. Today*, 2000, **16**, 469–476.
7 F. Kateera, C. M. Ingabire, E. Hakizimana, P. Kalinda, P. F. Mens, M. P. Grobusch, L. Mutesa and M. Van Vugt, Malaria, anaemia and under-nutrition: Three frequently co-existing conditions among preschool children in rural Rwanda, *Malar. J.*, 2015, **14**, 440.
8 N. Taparia, K. C. Platten, K. B. Anderson and N. J. Sniadecki, A microfluidic approach for hemoglobin detection in whole blood, *AIP Adv.*, 2017, **7**, 105102.
9 M. H. Antonelou, A. G. Kriebardis, A. D. Velentzas, A. C. Kokkalis, S. C. Georgakopoulou and I. S. Papassideri, Oxidative stress-associated shape transformation and membrane proteome remodeling in erythrocytes of end stage renal disease patients on hemodialysis, *J. Proteomics*, 2011, **74**, 2441–2452.
10 G. M. Rodgers, P. S. Becker, M. Blinder, D. Cella, A. Chanan-Khan, C. Cleeland, P. F. Coccia, B. Djulbegovic, J. A. Gilreath, E. H. Kraut, U. A. Matulonis, M. M. Millenson, D. Reinke, J. Rosenthal, R. N. Schwartz, G. Soff, R. S. Stein, G. Vlahovic and A. B. Weir, Cancer- and chemotherapy-induced anemia: Clinical practice guidelines in oncology, *J. Natl. Compr. Cancer Network*, 2012, **10**, 628–653.
11 Y. M. Serebrennikova, D. E. Huffman and L. H. Garcia-Rubio, Characterization of Red Blood Cells with Multiwavelength Transmission Spectroscopy, *BioMed Res. Int.*, 2015, **2015**, 1–11.
12 T. Wu and J. J. Feng, Simulation of malaria-infected red blood cells in microfluidic channels: Passage and blockage, *Biomicrofluidics*, 2013, **7**, 044115.
13 S. M. Hosseini and J. J. Feng, How malaria parasites reduce the deformability of infected red blood cells, *Biophys. J.*, 2012, **103**, 1–10.
14 G. Tomaiuolo, Biomechanical properties of red blood cells in health and disease towards microfluidics, *Biomicrofluidics*, 2014, **8**, 051501.
15 K. D. Barabino GA and M. O. Platt, Sickle cell biomechanics, *Annu. Rev. Biomed. Eng.*, 2010, **12**, 67.
16 L. Da Costa, J. Galimand, O. Fenneteau and N. Mohandas, Hereditary spherocytosis, elliptocytosis, and other red cell membrane disorders, *Blood Rev.*, 2013, **27**, 167–178.
17 A. V. Buys, M. J. Van Rooy, P. Soma, D. Van Papendorp, B. Lipinski and E. Pretorius, Changes in red blood cell membrane structure in type 2 diabetes: A scanning electron and atomic force microscopy study, *Cardiovasc. Diabetol.*, 2013, **12**, 25.
18 A. Vayá, L. Rivera, R. De La Espriella, F. Sanchez, M. Suescun, J. L. Hernandez and L. Fácila, Red blood cell distribution width and erythrocyte deformability in patients with acute myocardial infarction, *Clin. Hemorheol. Microcirc.*, 2015, **59**, 107–114.
19 G. Di Caprio, C. Stokes, J. M. Higgins, E. Schonbrun and D. A. Weitz, Single-cell measurement of red blood cell oxygen affinity, *Proc. Natl. Acad. Sci. U. S. A.*, 2015, **112**, 9984–9989.
20 S. M. Tsui, R. Ahmed, N. Amjad, I. Ahmed, J. Yang, F. A. M. Manno, I. Barman, W.-C. Shih and C. Lau, Single red blood cell analysis reveals elevated hemoglobin in poikilocytes, *J. Biomed. Opt.*, 2020, **25**, 1.
21 G. Rusciano, A. De Luca, G. Pesce and A. Sasso, Raman Tweezers as a Diagnostic Tool of Hemoglobin-Related Blood Disorders, *Sensors*, 2008, **8**, 7818–7832.
22 S. R. Memon, G. H. Brohi, F. R. Memon, M. Y. Shahani and S. Memon, Study on red cell distribution width, haematocrit and red blood corpuscle (RBC) indices are early markers for the detection of coronary artery disease: a case control study, *Prof. Med. J.*, 2019, **26**, 2075–2079.
23 R. Huisjes, A. Bogdanova, W. W. van Solinge, R. M. Schiffelers, L. Kaestner and R. van Wijk, Squeezing for Life – Properties of Red Blood Cell Deformability, *Front. Physiol.*, 2018, **9**, 1–22.
24 X. Li, M. Dao, G. Lykotrafitis and G. E. Karniadakis, Biomechanics and biorheology of red blood cells in sickle cell anemia, *J. Biomech.*, 2017, **50**, 34–41.
25 J. Jung, L. E. Matemba, K. Lee, P. E. Kazyoba, J. Yoon, J. J. Massaga, K. Kim, D. J. Kim and Y. Park, Optical characterization of red blood cells from individuals with

sickle cell trait and disease in Tanzania using quantitative phase imaging, *Sci. Rep.*, 2016, **6**, 1–9.

26 A. Larsson, L. Carlsson, B. Karlsson and M. Lipcsey, Rapid testing of red blood cell parameters in primary care patients using HemoScreen™ point of care instrument, *BMC Fam. Pract.*, 2019, **20**, 77.

27 J. Punter-Villagrasa, J. Cid, C. Páez-Avilés, I. Rodríguez-Villarreal, E. Juanola-Feliu, J. Colomer-Farrarons and P. L. Miribel-Català, An instantaneous low-cost point-of-care anemia detection device, *Sensors*, 2015, **15**, 4564–4577.

28 O. Oladele, O. Olatunde, O. Abiola, A. Oyinkansola, O. Evelyn, A. Babajide, O. Kehinde and O. Oyeku, Point-of-Care Testing for Anaemia in Children Using Portable Haematocrit Meter: A Pilot Study from Southwest Nigeria and Implications for Developing Countries, *Ethiop. J. Health Sci.*, 2016, **26**, 251.

29 S. Ilyas, A. E. Simonson and W. Asghar, Emerging point-of-care technologies for sickle cell disease diagnostics, *Clin. Chim. Acta*, 2020, **501**, 85–91.

30 P. T. McGann and C. Hoppe, The pressing need for point-of-care diagnostics for sickle cell disease: A review of current and future technologies, *Blood Cells, Mol., Dis.*, 2017, **67**, 104–113.

31 X. Huang, D. Xu, J. Chen, J. Liu, Y. Li, J. Song, X. Ma and J. Guo, Smartphone-based analytical biosensors, *Analyst*, 2018, **143**, 5339–5351.

32 S. Zhang, Z. Li and Q. Wei, Smartphone-based cytometric biosensors for point-of-care cellular diagnostics, *Nanotechnol. Precis. Eng.*, 2020, **3**, 32–42.

33 H. Zhu, S. O. Isikman, O. Mudanyali, A. Greenbaum and A. Ozcan, Optical Imaging Techniques for Point-of-care Diagnostics, *Lab Chip*, 2013, **13**, 51–67.

34 P. Gordon, V. P. Venancio, S. U. Mertens-Talcott and G. Coté, Portable bright-field, fluorescence, and cross-polarized microscope toward point-of-care imaging diagnostics, *J. Biomed. Opt.*, 2019, **24**, 1.

35 S. Ilyas, A. E. Simonson and W. Asghar, Emerging point-of-care technologies for sickle cell disease diagnostics, *Clin. Chim. Acta*, 2020, **501**, 85–91.

36 D. E. Discher, N. Mohandas and E. A. Evans, Molecular maps of red cell deformation: Hidden elasticity and in situ connectivity, *Science*, 1994, **266**, 1032–1035.

37 R. M. Hochmuth, Micropipette aspiration of living cells, *J. Biomech.*, 2000, **33**, 15–22.

38 E. A. Evans, New Membrane Concept Applied to the Analysis of Fluid Shear- and Micropipette-Deformed Red Blood Cells, *Biophys. J.*, 1973, **13**, 941–954.

39 G. Bao and S. Suresh, *Nat. Mater.*, 2003, **2**, 715–725.

40 M. M. Brandao, A. Fontes, M. L. Barjas-Castro, L. C. Barbosa, F. F. Costa, C. L. Cesar and S. T. O. Saad, Optical tweezers for measuring red blood cell elasticity: application to the study of drug response in sickle cell disease, *Eur. J. Haematol.*, 2003, **70**, 207–211.

41 H. Zhang and K. K. Liu, Optical tweezers for single cells, *J. R. Soc., Interface*, 2008, **5**, 671–690.

42 A. C. De Luca, G. Rusciano, R. Ciancia, V. Martinelli, G. Pesce, B. Rotoli, L. Selvaggi and A. Sasso, Spectroscopical and mechanical characterization of normal and thalassemic red blood cells by Raman Tweezers, *Opt. Express*, 2008, **16**, 7943.

43 J. P. Mills, L. Qie, M. Dao, C. T. Lim and S. Suresh, Nonlinear elastic and viscoelastic deformation of the human red blood cell with optical tweezers, *Mech. Chem. Biosyst.*, 2004, **1**, 169–180.

44 S. Hénon, G. Lenormand, A. Richert and F. Gallet, A new determination of the shear modulus of the human erythrocyte membrane using optical tweezers, *Biophys. J.*, 1999, **76**, 1145–1151.

45 H. Engelhardt, H. Gaub and E. Sackmann, Viscoelastic properties of erythrocyte membranes in high-frequency electric fields, *Nature*, 1984, **307**, 378–380.

46 K. E. Bremmell, A. Evans and C. A. Prestidge, Deformation and nano-rheology of red blood cells: An AFM investigation, *Colloids Surf., B*, 2006, **50**, 43–48.

47 Y. Zhang, C. Huang, S. Kim, M. Golkaram, M. W. A. Dixon, L. Tilley, J. Li, S. Zhang and S. Suresh, Multiple stiffening effects of nanoscale knobs on human red blood cells infected with *Plasmodium falciparum* malaria parasite, *Proc. Natl. Acad. Sci.*, 2015, **112**, 6068–6073.

48 L. A. Wilbur, M. J. Fletcher and D. A. Rosenbluth, Chemotherapy exposure increases leukemia cell stiffness, *Blood*, 2007, **109**, 3505–3508.

49 A. Sinha, T. T. T. Chu, M. Dao and R. Chandramohanadas, Single-cell evaluation of red blood cell bio-mechanical and nano-structural alterations upon chemically induced oxidative stress, *Sci. Rep.*, 2015, **5**, 9768.

50 Y. S. Nagornov and R. A. Pahomova, Atomic force microscopy of the erythrocyte membrane in obstructive jaundice, *Biophysics*, 2016, **61**, 405–412.

51 F. Liu, J. Burgess, H. Mizukami and A. Ostafin, Sample Preparation and Imaging of Erythrocyte Cytoskeleton with the Atomic Force Microscopy, *Cell Biochem. Biophys.*, 2003, **38**, 251–270.

52 H. Shi, Z. Liu, A. Li, J. Yin, A. G. L. Chong, K. S. W. Tan, Y. Zhang and C. T. Lim, Life Cycle-Dependent Cytoskeletal Modifications in Plasmodium falciparum Infected Erythrocytes, *PLoS One*, 2013, **8**, e61170.

53 G. V. Richieri, S. P. Akeson and H. C. Mel, Measurement of biophysical properties of red blood cells by resistance pulse spectroscopy: volume, shape, surface area, and deformability, *J. Biochem. Biophys. Methods*, 1985, **11**, 117–131.

54 E. Schonbrun, R. Malka, G. Di Caprio, D. Schaak and J. M. Higgins, Quantitative absorption cytometry for measuring red blood cell hemoglobin mass and volume, *Cytometry, Part A*, 2014, **85**, 332–338.

55 G. Popescu, Y. Park, R. R. Dasari, K. Badizadegan and M. S. Feld, Coherence properties of red blood cell membrane motions, *Phys. Rev. E: Stat., Nonlinear, Soft Matter Phys.*, 2007, **76**, 28–32.

56 G. Popescu, T. Ikeda, K. Goda, C. A. Best-Popescu, M. Laposata, S. Manley, R. R. Dasari, K. Badizadegan and M. S. Feld, Optical measurement of cell membrane tension, *Phys. Rev. Lett.*, 2006, **97**, 218101.

57 Y. Park, C. A. Best, K. Badizadegan, R. R. Dasari, M. S. Feld, T. Kuriabova, M. L. Henle, A. J. Levine and G. Popescu, Measurement of red blood cell mechanics during morphological changes, *Proc. Natl. Acad. Sci.*, 2010, **107**, 6731–6736.

58 T. Betz, M. Lenz, J. F. Joanny and C. Sykes, ATP-dependent mechanics of red blood cells, *Proc. Natl. Acad. Sci. U. S. A.*, 2009, **106**, 15320–15325.

59 R. Zhang and F. L. H. Brown, Cytoskeleton mediated effective elastic properties of model red blood cell membranes, *J. Chem. Phys.*, 2008, **129**, 065101.

60 S. E. Leblanc, *The Influence of Red Blood Cell Scattering In Optical Pathways of Retinal Vessel Oximetry*, 2011, p. 197.

61 Y. Zheng, J. Nguyen, Y. Wei and Y. Sun, Recent advances in microfluidic techniques for single-cell biophysical characterization, *Lab Chip*, 2013, **13**, 2464–2483.

62 M. Abkarian, M. Faivre, R. Horton, K. Smistrup, C. A. Best-Popescu and H. A. Stone, Cellular-scale hydrodynamics, *Biomed. Mater.*, 2008, **3**, 034011.

63 G. Tomaiuolo, M. Barra, V. Preziosi, A. Cassinese, B. Rotoli and S. Guido, Microfluidics analysis of red blood cell membrane viscoelasticity, *Lab Chip*, 2011, **11**, 449–454.

64 M. Razizadeh, M. Nikfar, R. Paul and Y. Liu, Coarse-Grained Modeling of Pore Dynamics on the Red Blood Cell Membrane under Large Deformations, *Biophys. J.*, 2020, **119**, 471–482.

65 M. Nikfar, M. Razizadeh, R. Paul and Y. Liu, Multiscale modeling of hemolysis during microfiltration, *Microfluid. Nanofluid.*, 2020, **24**, 33.

66 M. Nikfar, M. Razizadeh, J. Zhang, R. Paul, Z. J. Wu and Y. Liu, Prediction of mechanical hemolysis in medical devices via a Lagrangian strain-based multiscale model, *Artif. Organs*, 2020, **44**, 348–368.

67 G. Popescu, T. Ikeda, R. R. Dasari and M. S. Feld, Diffraction phase microscopy for quantifying cell structure and dynamics, *Opt. Lett.*, 2006, **31**, 775.

68 G. Popescu, K. Badizadegan, R. R. Dasari and M. S. Feld, Observation of dynamic subdomains in red blood cells, *J. Biomed. Opt.*, 2006, **11**, 040503.

69 G. Popescu, T. Ikeda, C. A. Best, K. Badizadegan, R. R. Dasari and M. S. Feld, Erythrocyte structure and dynamics quantified by Hilbert phase microscopy, *J. Biomed. Opt.*, 2005, **10**, 060503.

70 Y. Kaizuka and J. T. Groves, Hydrodynamic damping of membrane thermal fluctuations near surfaces imaged by fluorescence interference microscopy, *Phys. Rev. Lett.*, 2006, **96**, 118101.

71 F. Brochard, J. F. Lennon and I. N. Erythrocytes, Frequency spectrum of the flicker phenomenon in erythrocytes, *J. Phys.*, 1975, **36**, 1035–1047.

72 A. Zilker, M. Ziegler and E. Sackmann, Spectral analysis of erythrocyte flickering in the 0.3-4- microm-1 regime by microinterferometry combined with fast image processing, *Phys. Rev. A: At., Mol., Opt. Phys.*, 1992, **46**, 7998–8001.

73 S. Tuvia, S. Levin, A. Bitler and R. Korenstein, Mechanical fluctuations of the membrane-skeleton are dependent on F- actin ATPase in human erythrocytes, *J. Cell Biol.*, 1998, **141**, 1551–1561.

74 M. Mir, K. Tangella and G. Popescu, Blood testing at the single cell level using quantitative phase and amplitude microscopy, *Biomed. Opt. Express*, 2011, **2**, 3259.

75 K. Jaferzadeh, I. Moon, M. Bardyn, M. Prudent, J.-D. Tissot, B. Rappaz, B. Javidi, G. Turcatti and P. Marquet, Quantification of stored red blood cell fluctuations by time-lapse holographic cell imaging, *Biomed. Opt. Express*, 2018, **9**, 4714.

76 B. Javidi, A. Markman, S. Rawat, T. O'Connor, A. Anand and B. Andemariam, Sickle cell disease diagnosis based on spatio-temporal cell dynamics analysis using 3D printed shearing digital holographic microscopy, *Opt. Express*, 2018, **26**, 13614.

77 N. L. Swanson, B. D. Billard and T. L. Gennaro, Limits of optical transmission measurements with application to particle sizing techniques, *Appl. Opt.*, 1999, **38**, 5887.

78 R. Barer and S. Tkaczyk, Refractive index of concentrated protein solutions, *Nature*, 1954, **173**, 821–822.

79 M. L. Gray, R. A. Hoffman and W. P. Hansen, A new method for cell volume measurement based on volume exclusion of a fluorescent dye, *Cytometry*, 1983, **3**, 428–434.

80 T. Betz and C. Sykes, Time resolved membrane fluctuation spectroscopy, *Soft Matter*, 2012, **8**, 5317–5326.

81 B. Fröhlich, J. Jäger, C. Lansche, C. P. Sanchez, M. Cyrklaff, B. Buchholz, S. T. Soubeiga, J. Simpore, H. Ito, U. S. Schwarz, M. Lanzer and M. Tanaka, Hemoglobin S and C affect biomechanical membrane properties of P. falciparum-infected erythrocytes, *Commun. Biol.*, 2019, **2**, 311.

82 Y. Z. Yoon, H. Hong, A. Brown, C. K. Dong, J. K. Dae, V. L. Lew and P. Cicuta, Flickering analysis of erythrocyte mechanical properties: Dependence on oxygenation level, cell shape, and hydration level, *Biophys. J.*, 2009, **97**, 1606–1615.

83 N. S. Gov and S. A. Safran, Red blood cell membrane fluctuations and shape controlled by ATP-induced cytoskeletal defects, *Biophys. J.*, 2005, **88**, 1859–1874.

84 L. Mandel and E. Wolf, Coherence properties of optical fields, *Rev. Mod. Phys.*, 1965, **37**, 231–287.

85 L. Mandel and E. Wolf, *Optical Coherence and Quantum Optics, Second-order coherence theory of scalar wavefields*, Cambridge university press, 1995, vol. 64, Ch. 4.

86 J. P. Hale, G. Marcelli, K. H. Parker, C. P. Winlove and P. G. Petrov, Red blood cell thermal fluctuations: Comparison between experiment and molecular dynamics simulations, *Soft Matter*, 2009, **5**, 3603–3606.

87 J. Evans, W. Gratzer, N. Mohandas, K. Parker and J. Sleep, Fluctuations of the red blood cell membrane: Relation to mechanical properties and lack of ATP dependence, *Biophys. J.*, 2008, **94**, 4134–4144.

88 N. Z. Piety, W. H. Reinhart, P. H. Pourreau, R. Abidi and S. S. Shevkoplyas, Shape matters: The effect of red blood cell shape on perfusion of an artificial microvascular network, *Transfusion*, 2016, **56**, 844–851.

89 J. W. Harvey, *The Erythrocyte: Physiology, Metabolism, and Biochemical Disorders*, Elsevier, 1997.
90 R. Skalak and P. I. Branemark, Deformation of red blood cells in capillaries, *Science*, 1969, **164**, 717–719.
91 Y. Kim, H. Shim, K. Kim, H. J. Park, S. Jang and Y. K. Park, Profiling individual human red blood cells using common-path diffraction optical tomography, *Sci. Rep.*, 2014, **4**, 1–7.
92 S. Tuvia, A. Almagor, A. Bitler, S. Levin, R. Korenstein and S. Yedgar, Cell membrane fluctuations are regulated by medium macroviscosity: Evidence for a metabolic driving force, *Proc. Natl. Acad. Sci. U. S. A.*, 1997, **94**, 5045–5049.
93 M. C. Stankewich, W. T. Tse, L. L. Peters, Y. Ch'ng, K. M. John, P. R. Stabach, P. Devarajan, J. S. Morrow and S. E. Lux, A widely expressed βIII spectrin associated with Golgi and cytoplasmic vesicles, *Proc. Natl. Acad. Sci. U. S. A.*, 1998, **95**, 14158–14163.
94 Y. K. Park, C. A. Best, T. Auth, N. S. Gov, S. A. Safran, G. Popescu, S. Suresh and M. S. Feld, Metabolic remodeling of the human red blood cell membrane, *Proc. Natl. Acad. Sci. U. S. A.*, 2010, **107**, 1289–1294.
95 R. Rodríguez-García, I. López-Montero, M. Mell, G. Egea, N. S. Gov and F. Monroy, Direct Cytoskeleton Forces Cause Membrane Softening in Red Blood Cells, *Biophys. J.*, 2015, **108**, 2794–2806.
96 J. Evans, W. Gratzer, N. Mohandas, K. Parker and J. Sleep, Fluctuations of the red blood cell membrane: Relation to mechanical properties and lack of ATP dependence, *Biophys. J.*, 2008, **94**, 4134–4144.
97 E. Evans, N. Mohandas and A. Leung, Static and dynamic rigidities of normal and sickle erythrocytes. Major influence of cell hemoglobin concentration, *J. Clin. Invest.*, 1984, **73**, 477–488.
98 Y. Kim, K. Kim and Y. Park, in *Blood Cell - An Overview of Studies in Hematology*, InTech, 2012.